NANO LETTERS

pubs.acs.org/NanoLett

Letter

Metal-Free Oxide-Nitride Heterostructure as a Tunable Hyperbolic Metamaterial Platform

Xuejing Wang, Haohan Wang, Jie Jian, Bethany X. Rutherford, Xingyao Gao, Xiaoshan Xu, Xinghang Zhang, and Haiyan Wang*

Cite This: *Nano Lett.* 2020, 20, 6614−6622

Read Online

ACCESS | Metrics & More | Article Recommendations | Supporting Information

ABSTRACT: Metal-free plasmonic metamaterials with wide-range tunable optical properties are highly desired for various components in future integrated optical devices. Designing a ceramic−ceramic hybrid metamaterial has been theoretically proposed as a solution to this critical optical material demand. However, the processing of such all-ceramic metamaterials is challenging due to difficulties in integrating two very dissimilar ceramic phases as one hybrid system. In this work, an oxide-nitride hybrid metamaterial combining two highly dissimilar ceramic phases, i.e., semiconducting weak ferromagnetic NiO nanorods and conductive plasmonic TiN matrix, has been successfully integrated as a unique vertically aligned nanocomposite form. Highly anisotropic optical properties such as hyperbolic dispersions and strong magneto-optical coupling have been demonstrated under room temperature. The novel functionalities presented show the strong potentials of this new ceramic−ceramic hybrid thin film platform and its future applications in next-generation nanophotonics and magneto-optical integrated devices without the lossy metallic components.

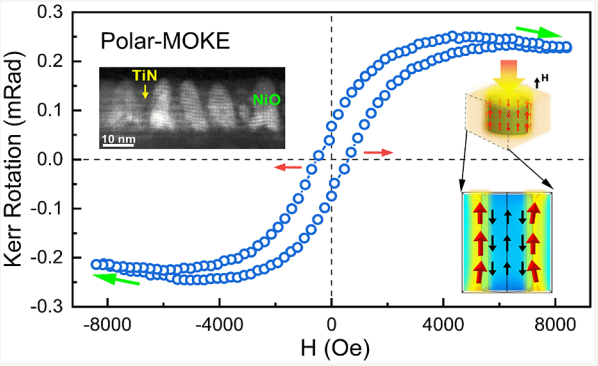

KEYWORDS: *oxide-nitride heterostructure, hyperbolic metamaterial, titanium nitride, ferromagnetic nanostructure, magneto-optical coupling, Kerr rotation*

INTRODUCTION

Metamaterials with artificially designed nanostructures or meta-atoms at subwavelength scale have attracted extensive research interests toward new physics phenomena and controllable metadevices in practical.[1,2] Coupled with studies of plasmonics, this rising field of study brings tremendous opportunities in engineerable plasmonic metamaterials that realize properties such as extreme electromagnetic (EM) field localization and enhancement, sensing, and subdiffraction imaging.[3−6] Among the various types of metamaterials, a hyperbolic metamaterial with coupled surface plasmons (SPs) confined at the interface between typically a metal and a dielectric becomes precedingly favorable in manipulating light−matter interactions in an effective way.[7,8] The primary reason for coupling dissimilar materials is to generate highly anisotropic dielectric tensors which is usually represented by hyperbolic isofrequency surfaces opposed to the spherical ones as commonly seen in conventional materials. Such anisotropy can be further tuned to achieve enhanced nonlinearity, negative refraction, as well as controllable hyperbolic dispersion at different wavelength regions.[9,10]

However, metallic meta-atoms usually lead to optical losses and material instabilities that hinder the metadevice applications under harsh environmental conditions.[11−13] Thus, seeking plasmonic candidates with lower loss and higher durability becomes crucial from the fundamental perspective. Recent explorations suggest that materials such as graphene and ceramics (e.g., doped oxides, transition metal nitrides) could be alternative options.[14−17] For example, titanium nitride (TiN) exhibits comparable plasmonic properties with Au but possesses lower losses and higher endurance upon thermal or laser treatment.[18,19] In addition, all-dielectric metasurfaces have been proposed with low-loss electromagnetic properties, which are capable of extending the effective permittivity into all four quadrants.[20] Among the dielectric ceramics, a wide range of candidates (e.g., oxides, nitrides, carbides) can be considered which provide tunable properties including charge carrier density, refractive indices, or other EM properties. Therefore, it is possible to realize all-ceramic hyperbolic metamaterials at nanoscale. However, due to the fact of potential interaction or intermixing between the cations as well

Received: June 11, 2020
Revised: July 26, 2020
Published: July 27, 2020

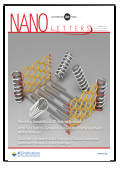

https://dx.doi.org/10.1021/acs.nanolett.0c02440
Nano Lett. 2020, 20, 6614−6622

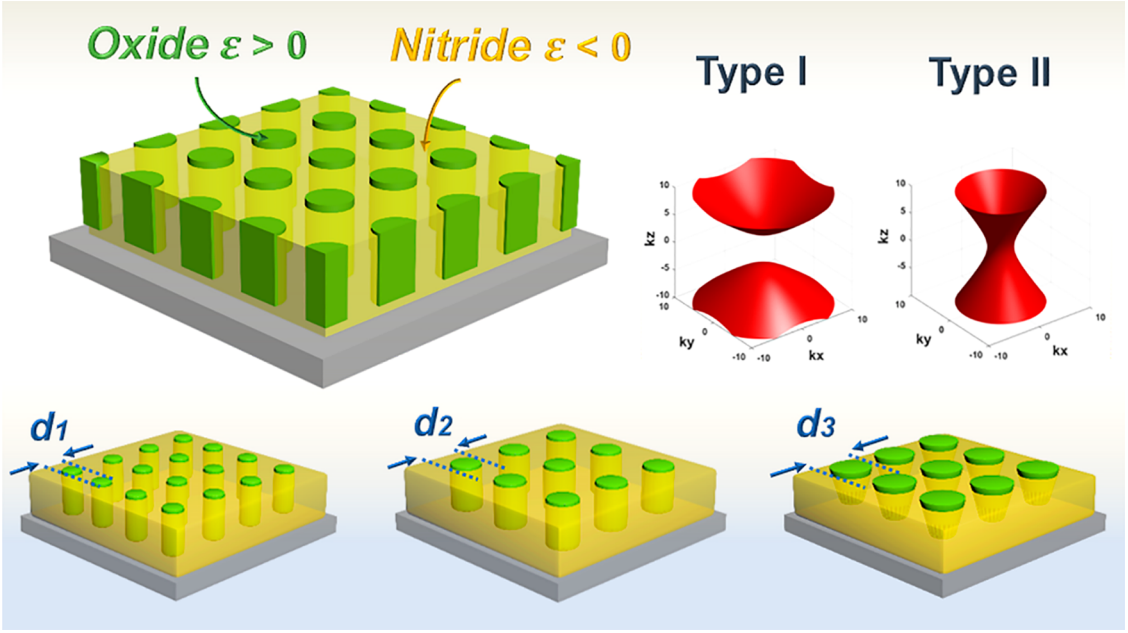

Figure 1. Conceptual illustration on a ceramic−ceramic (oxide−nitride) hyperbolic metamaterial. Ferromagnetic oxide nanorods embedded in a plasmonic nitride matrix showing hyperbolic dispersion. The nanorod diameter can be tailored systematically.

as deficiency of anions of the constituent ceramic phases, the experimental demonstration of the as-proposed ceramic−ceramic metamaterials is challenging and scarcely reported.

In this work, an oxide−nitride hybrid metamaterial combining two highly dissimilar ceramic phases, i.e., semiconducting magnetic nickel oxide (NiO) and conductive plasmonic titanium nitride (TiN), has been demonstrated as a unique vertically aligned nanocomposite (VAN) configuration. As illustrated in Figure 1, the heterostructure is composed of vertically aligned nanorods of NiO with the TiN matrix; the dimension of the nanorods can be tailored systematically (Figure 1, lower pane). The selection of TiN and NiO is based on the following factors: (1) TiN possesses a good plasmonic property and high density of electrons and exhibits a paramagnetic property at room temperature. (2) NiO is an intrinsic p-type semiconductor and generally exhibits an antiferromagnetic property,[21,22] whereas nanostructured NiO with domain size ranging from 5 to 200 nm has been reported with a weak ferromagnetic response.[23−25] (3) Both materials are cubic with lattice parameters of a_{TiN} = 4.241 Å and a_{NiO} = 4.175 Å, respectively, and both can epitaxially grow on MgO (a_{MgO} = 4.211 Å).

It is expected that the integration and coupling of nanodomains of NiO with TiN could lead to several unique features: (1) TiN as a refractory low-loss plasmonic matrix supports strong SP modes. (2) NiO as a nanorod array enhances the ferromagnetic response and provides additional tunability. (3) A strong variation of dielectric (ε) dispersion at optical frequencies can be induced by coupling ε-positive NiO with ε-negative TiN. (4) The magneto-optical (MO) coupling of surface plasmons (SPs) with magnetic spins at the TiN/NiO interface. Benefiting from the ultrafast switching properties of both magnetic and optical modes,[26−30] the hybrid film can potentially realize a dynamic control of metamaterial devices using external stimuli.

RESULTS AND DISCUSSION

The growth of a hybrid NiO−TiN thin film was approached using pulsed laser deposition (PLD). To avoid interdiffusion or chemical interaction, the deposition was carried under high vacuum. While a single-crystalline TiN film with 1:1 stoichiometry has already been demonstrated,[31,32] oxide films grown under a reduced oxygen atmosphere could potentially introduce oxygen vacancies or phase segregation.[33,34] The quality of film was first explored using X-ray diffraction (XRD); θ−2θ scans are displayed in Figure S1. Here, the pure NiO (expected 1:1) film grown under O_2 was measured as a reference. The NiO (002) peak is located at 43.45° (a = 4.160 Å) which is under slight compression out-of-plane as compared to its bulk value of 43.29° (4.175 Å). In terms of the hybrid NiO−TiN film, two shoulder peaks located close to the MgO (002) substrate peak are identified as TiN (002) on the left and NiO (002) on the right. This indicates that desirable lattice matching and strain coupling are expected at both the NiO/TiN interface and the film/substrate interface, which serve as the premise for the high-quality VAN integration with well-separated phase boundaries. It is worth noting that Ni (111) at 44.507° and Ni (002) at 51.846° are not noticeable, which indicate that NiO is grown without phase segregation.

The microstructure was probed by scanning transmission electron microscopy (STEM) and energy-dispersive X-ray spectroscopy (EDX). As visualized from the high-angle annular dark-field (HAADF) STEM and EDX mapping shown in Figure 2, the hypothesis of the nanorod-in-matrix morphology is achieved. Figure 2b-1 displays a local cross-sectional projection of the film, where the NiO phase is grown as distinct rods without interdiffusion. It is noted that the film thickness in the presented sample is 18 nm, which can be further tuned by controlling deposition time.[35,36] Interestingly, a Moiré pattern is observed especially inside the nanorods, indicating a strained condition of nanostructured NiO. The sharp phase boundaries are confirmed by EDX mapping in Figure 2b-2, where the NiO/TiN and film/substrate

https://dx.doi.org/10.1021/acs.nanolett.0c02440
Nano Lett. 2020, 20, 6614−6622

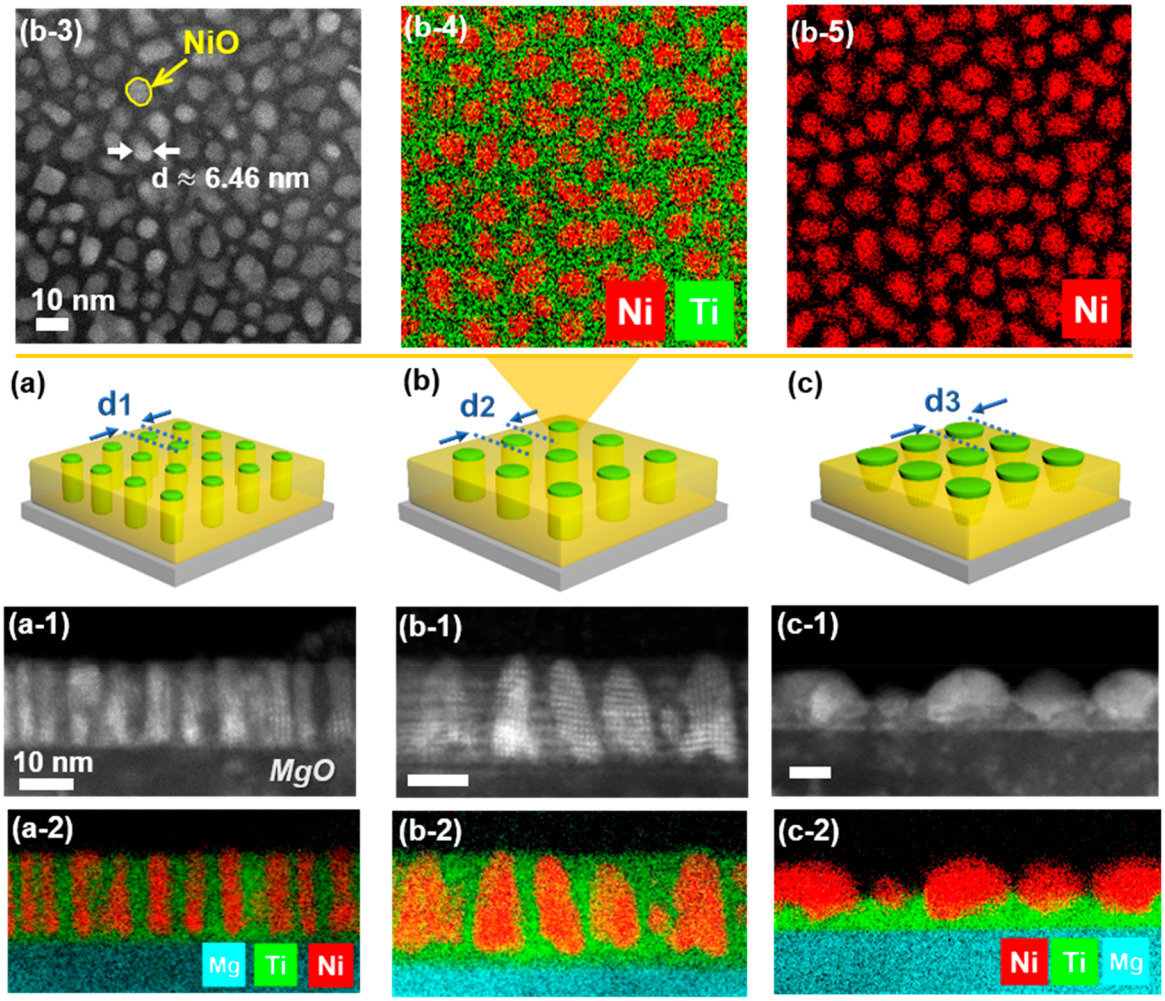

Figure 2. (a–c) Schematic illustrations of NiO–TiN VANs with increasing diameter of NiO nanorods. (a-1–c-1) Cross-sectional STEM images of corresponding nanostructures grown at 10 Hz, 5 Hz and 2 Hz laser frequency. (a-2–c-2) EDX elemental mapping of Mg, Ti, and Ni. (b-3) Plan-view STEM micrograph of NiO–TiN (5 Hz) and (b-4, b-5) corresponding EDX mapping.

boundaries are clearly visualized. Plan-view STEM micrograph and EDX mapping are displayed in Figure 2b-3–5), which confirm a uniform distribution of NiO nanorods in the TiN matrix. The areas with a brighter contrast correspond to NiO nanorods due to a higher Z (atomic number) of Ni as compared to Ti. It is noted that the boundaries of the NiO nanorods are irregular, i.e., neither round nor squared, possibly due to the minimization of surface energy during growth.[37]

The histogram based on the plan-view micrograph is displayed in Figure S2, resolving an average pillar diameter of 6.46 nm with an overall volume fraction of 33% in the presented sample (Figure 2b). Via careful tuning of the laser frequency, a systematic change of nanorod diameter is realized as shown from Figure 2a-1,2 for 10 Hz, Figure 2b-1,2 for 5 Hz, and Figure 2c-1,2 for 2 Hz laser frequency. As a comparison, the larger diameter of the nanorods in the 2 Hz film is due to a longer resting/diffusion time of adatoms during deposition that causes the enlarged NiO nucleus, while coarsening of the film surface is affected by the different growth rates between TiN and NiO. The 5 Hz sample with optimized surface roughness and dimension was selected for further measurements. In general, the nanorods are distributed uniformly over the entire sample, and the chemical compositions within three films are comparable as quantified by EDX mapping in scanning electron microscopy (SEM) (Figure S3 and Table S1). A brief illustration of the growth mechanism of the NiO-TiN VAN is shown in Figure S4, and related growth mechanism of other TiN-based VANs, such as TiN-Au and TiN-Ag, can be found in the previous reports.[38,39]

Optical and magnetic properties of the NiO–TiN VAN film are explored as both phases are highly functional. At 300–1500 nm, depolarized light transmittance (T, 0° incidence) and reflectance (R, 8° incidence) spectra of the hybrid NiO–TiN thin-film metamaterial are displayed in Figure 3a. Specifically, the resonance located at 500 nm for the transmission mode is red-shifted to 620 nm for the reflection mode. The metallic nature of TiN and the sub-20 nm film thickness resulted in low intensities (<50%) of both T and R spectra. A comparison between T spectra of NiO–TiN and pure NiO thin films is shown in Figure S5a, from which the band gap is roughly estimated based on the Tauc method (Figure S5b). There is a 0.168 eV band gap reduction as expected from an enhanced charge carrier density introduced by TiN. Next, a 10 nm × 10 nm unit cell composed of one nanorod (d = 6.46 nm) was modeled. The simulated optical spectra are displayed in Figure 3b. Aside from a blue shift of the resonances, the simulated spectra in general match well with the measurement. The minor inaccuracy of the simulation could be caused by the

https://dx.doi.org/10.1021/acs.nanolett.0c02440
Nano Lett. 2020, 20, 6614–6622

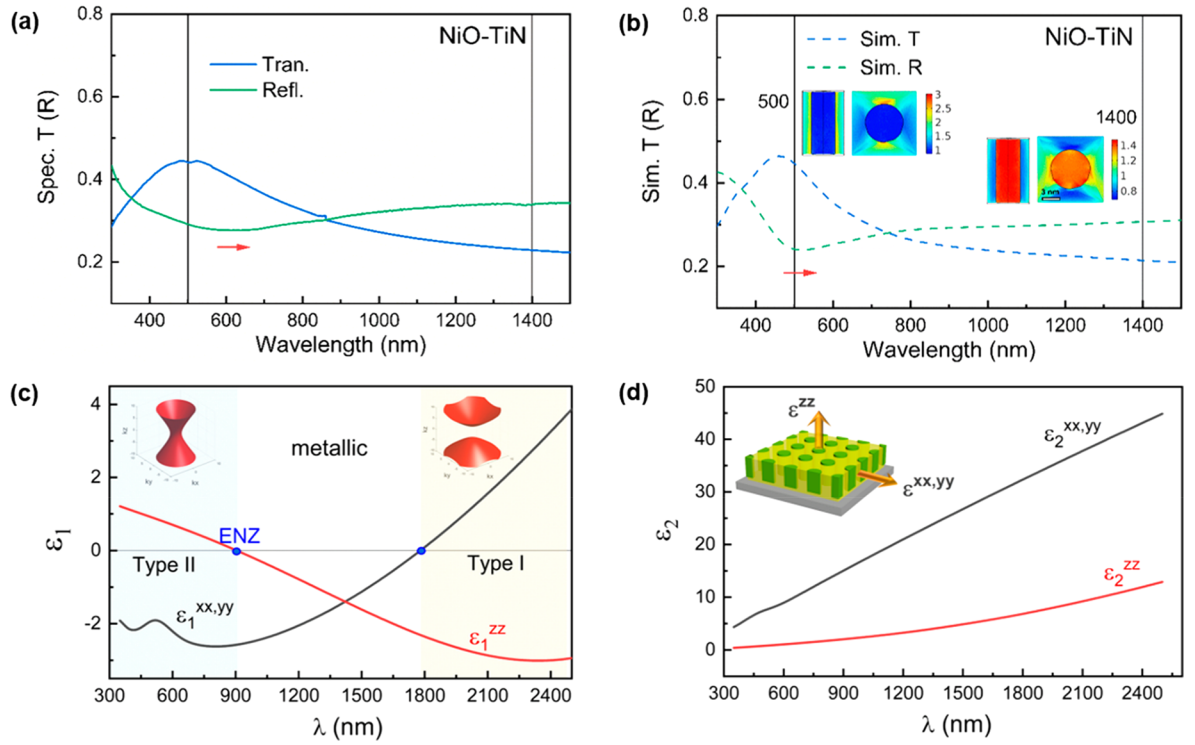

Figure 3. (a) Measured and (b) simulated transmittance and reflectance spectra of hybrid NiO−TiN film. Insets: electric field maps of top and side projections at 0.5 and 1.4 μm. (c) Real and (d) imaginary part dielectric constant of NiO−TiN film. Insets show *k*-space dispersion topologies at two wavelengths (0.5 and 2.1 μm).

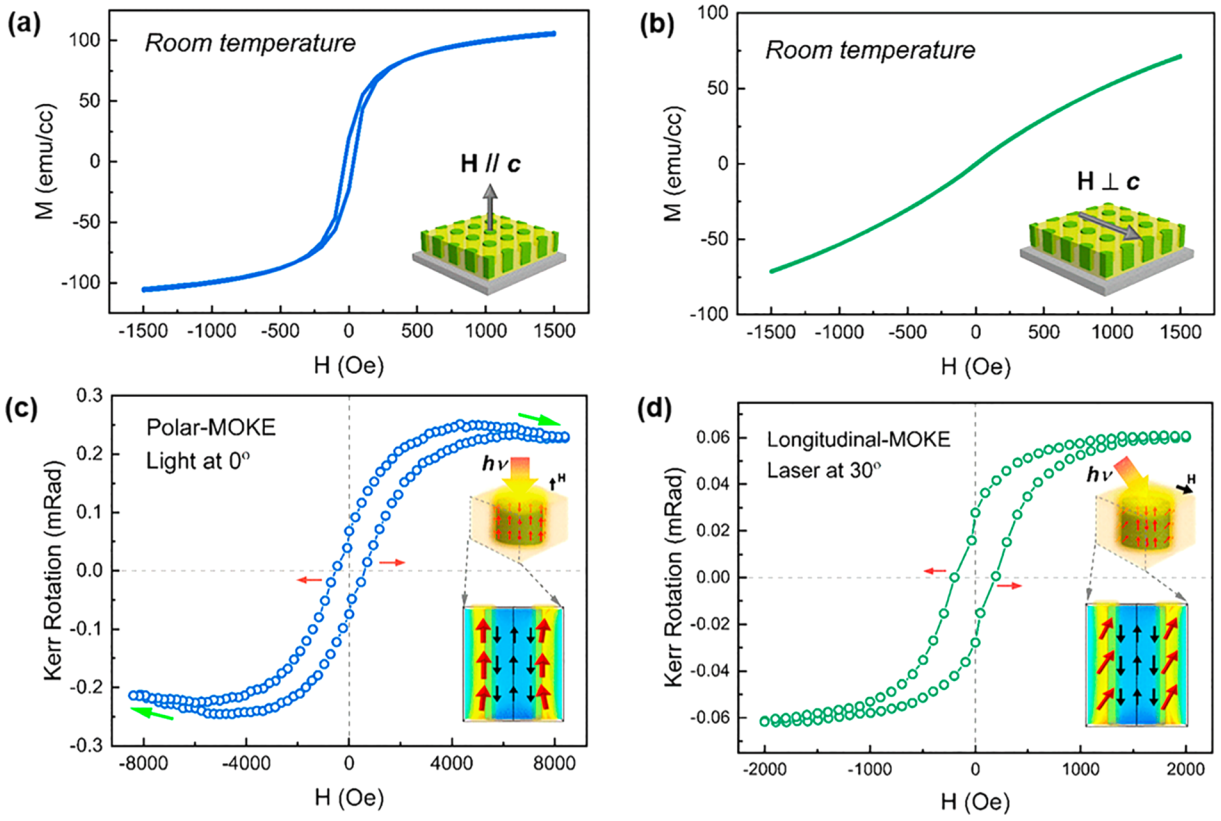

Figure 4. (a) Room temperature *M*−*H* loop for NiO−TiN film at the out-of-plane direction. (b) Room temperature *M*−*H* loop for NiO−TiN film at the in-plane direction. (c) Room temperature polar- and (d) longitudinal-Kerr rotation loops, laser wavelength is 632.8 nm. Insets show MOKE configuration and spin alignment cross-sections.

https://dx.doi.org/10.1021/acs.nanolett.0c02440
Nano Lett. 2020, 20, 6614−6622

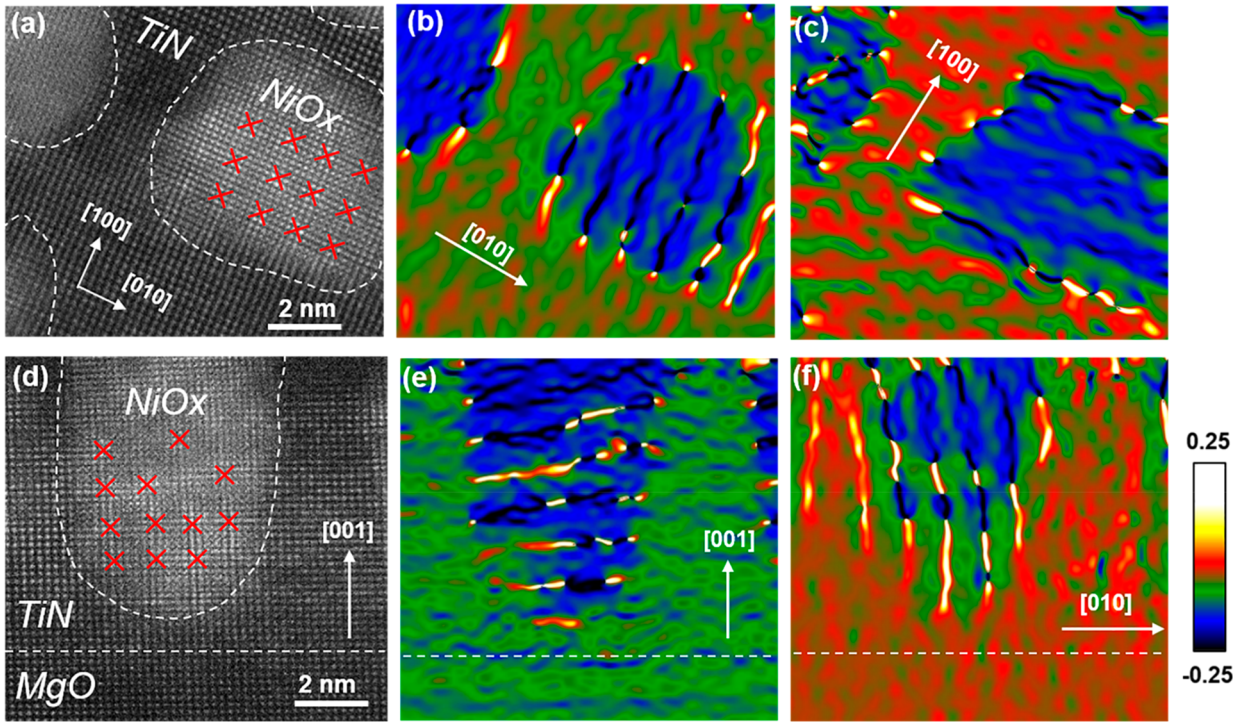

Figure 5. (a) Plan-view HRSTEM micrograph. (b, c) In-plane (ε_{xx}) strain map along [010] and [100]. (d) Cross-sectional HRSTEM micrograph. (e) Out-of-plane (ε_{yy}) strain map along [001]. (f) In-plane (ε_{xx}) strain map along [010].

inhomogeneity, scattering, or defects at the NiO/TiN boundaries. Insets of Figure 3b show the electric field maps at two selected wavelengths. At 500 nm, the field energy is localized at NiO/TiN interfaces. Here, the TiN matrix can be considered as a porous template where the holes are "filled by" NiO nanorods,[40,41] such that strong localized surface plasmon resonance (LSPR) and field localization at the edges of the TiN matrix are expected. Away from the resonance, the electric field is mostly localized inside NiO without much coupling at its interface.

Next, dielectric constant along in-plane ($\varepsilon^{xx} = \varepsilon^{yy} = \varepsilon^{o}$) and out-of-plane ($\varepsilon^{zz} = \varepsilon^{eo}$) directions are displayed in Figure 3c,d. Pure NiO film is expected to exhibit as a dielectric while pure TiN film shows metallic behavior in most optical frequencies.[38] Upon coupling, hyperbolic dispersions are observed in the measured frequencies. Specifically, the uniaxial tensors of the dielectric function with one-fold hyperboloid (type II, $\varepsilon_1^{xx,yy} < 0$, $\varepsilon_1^{zz} > 0$) are visualized from 350 to 900 nm, and 2-fold hyperboloid (type I $\varepsilon_1^{xx,yy} > 0$, $\varepsilon_1^{zz} < 0$) is observed at 1775 nm and above. The *k*-space topologies corresponding to 0.5 and 2.1 μm are shown as insets.[42] The epsilon-near-zero (ENZ) property as marked by blue circles indicates the dielectric−metallic transitions.[43] Between the two hyperbolic regions, the hybrid film remains effectively metallic considering that TiN plays a dominate role with its 67% filling factor. It is worth noting that the hyperbolic transition can be tuned by controlling the filling factor and diameter of NiO, or by exchanging metamaterial configuration. Fitted ellipsometric parameters and polarized reflectance spectra (R_{PP}, R_{SS}) of the NiO−TiN film are retrieved and displayed in Figure S5c−f.

As proposed, the nanostructured NiO could induce weak ferromagnetism at room temperature; here, the unbalanced spins at the boundaries of the nanorods can be aligned by the magnetic field. Room temperature magnetization hysteresis loops with magnetic field applied along out-of-plane (H//*c*) and in-plane (H⊥*c*) directions are displayed in Figure 4a,b. As a comparison, the magnetic moment along out-of-plane exhibits weak ferromagnetic behavior, while the in-plane direction is merely paramagnetic. Since the nanorods are vertical aligned, such anisotropy can be explained by a stronger coupling mode between spins and magnetic moment along the *c*-axis. Under low temperature (10 K), the ferromagnetism is enhanced, represented by both the coercive field (H_C) and the saturation moment (M_S) as shown in Figure S6a,b. The H_C (H//*c*) varies from 19.157 to 84.146 Oe, indicating a 3-fold increase. Aside from a stronger spin polarization, such enhancement could be potentially affected by the stoichiometry of NiO (1:*x*) resulted from vacuum growth.

Further, polar and longitudinal Kerr rotations with a change of magnetic field were recorded at room temperature to investigate the magneto-optical coupling. The enhanced MO effect requires minimizing polarized reflectance (R_{PP}) and/or maximizing polarization conversion (R_{PS}) as defined by the complex Kerr rotation Φ as $\Phi = \frac{R_{PS}}{R_{PP}}$.[29] Interestingly, the fitted R_{PP} (Figure S5e) indicates an extended surface plasmon resonance (SPP) in the range 350−750 nm (shaded area) that matches with the laser frequency of 632.8 nm; in addition, an enhanced electric field is generated (Figure 3b) at the NiO/TiN interface. For the polar configuration (Figure 4c), both the laser and magnetic field are applied at 0° incidence to the film surface, while for the longitudinal configuration (Figure 4d), the laser impinges at 30° while the magnetic field is applied along the in-plane direction. Here, enhanced Kerr rotation is realized in both polar and longitudinal modes, as evidenced by the coercive field opening marked by red arrows. For example, the H_C^{Kerr} of 626.314 Oe (Figure 4c) suggests a dramatic enhancement as compared to the H_C of 19.157 Oe in Figure 4a. This demonstrates a significant room-temperature spin polarization using light as an ultrafast stimulus, which is

https://dx.doi.org/10.1021/acs.nanolett.0c02440
Nano Lett. 2020, 20, 6614−6622

not achievable by tuning temperature or exciting pure NiO film (Figure S6).

To explain how a propagating EM field enhances the magnetic spin state, we use the 2D electric field maps of the NiO−TiN unit cell retrieved at 632.8 nm (Figure 4c,d). Black arrows indicate the AFM spins at the inner domain, and red arrows indicate the FM spins at the NiO domain boundary. These unbalanced spins at the boundary of the nanorod generate a weak ferromagnetism at room temperature, which can be further enhanced when light impinges onto the film surface. Specifically, a stronger MO effect is proposed in polar Kerr where the field energy at the vertical interface is strongly excited, which results in enhanced coupling and spin polarizations. For the longitudinal Kerr, the electric field propagating at 30° incidence decays faster, and the in-plane magnetic field provides weaker coupling at the vertical interface. This can be verified by comparing the saturation field (H_S) and the Kerr rotation from Figure 4c,d. Interestingly, under high fields (6000 Oe and beyond), the Polar Kerr rotation starts to reverse as indicated by the green arrows. Considering the AFM nature of NiO, it is proposed that, under high magnetic field, the spins at nanorod boundaries are completely polarized such that the inner AFM domain being probed acts as counteractive effect and reduces further enhancement of the Kerr signal. In general, these substantial variations by comparing the magnetometry hysteresis loops (Figure 4a,b) with MO Kerr loops (Figure 4c,d) suggest a correlation between both diagonal and off-diagonal terms of the dielectric function with the change of magnetic field,[29,44−46] which are valuable for further investigations. It is also noted that the coupling between diagonal dielectric tensors with magnetization of such hybrid metamaterial could be of great importance toward applications in ultrafast switching, magnetic storage, sensors, and circuit designs.[47,48]

To further understand the ceramic−ceramic metamaterial growth, geometric phase analysis (GPA) was applied to visualize the 3D strain state based on the high-resolution STEM (HRSTEM) micrographs displayed in Figure 5a,d. At the pillar/matrix interface, atomic sharp phase contrast is observed without subdomains or obvious distortion. Next, biaxial strains ε_{xx} (in-plane) and ε_{yy} (out-of-plane) are determined. Note that ε_{xx} includes two crystalline orientations, [010] and [100]. Relative strain from −25% to 25% as compared to the TiN lattice is displayed as color contours. From cross-section maps (Figure 5e,f), TiN and MgO maintain a low strain state (<0.1%) due to a close lattice matching in between. However, a drastic contrast is observed inside the pillars where the dark blue indicates a smaller lattice as compare to the TiN; thus, a tensile strain occurs in both ε_{xx} and ε_{yy}. Bright dots with lines threading through at the pillar edges suggest dislocation cores generated to partially compensate the strain. Interestingly, translational Moiré pattern (red crosses) with parallel mode indicates that two sets of lattices exist with misfit. It is proposed that NiO is under a metastable state; i.e., a small amount of oxygen deficiency of nanocrystal NiO_x could be possible which causes such a highly strained interface visualized in STEM. It is also possible that the high-energy (300 kV) electron beam of the STEM could induce such degradation.[49,50] We collected the atomic ratio of Ni and O based on the EDX mapping of low-magnification cross-sectional images (Table S2); a rough Ni:O ratio of 1:1 can be inferred for NiO. The exact stoichiometry could be important in tuning the dielectric function (Figure S7), which is valuable to explore in future studies. In general, the XRD results from a large sample area demonstrate a successful integration of the epitaxial NiO−TiN heterostructure.

The oxide-nitride artificial heterostructure presented here was fabricated by a self-assembling process, which offers flexible controls over pillar geometry and density such that the material morphology can be tuned as desired. Therefore, such two-phase metamaterials can be engineered for metadevice applications such as modulators, switches, or neuromorphic computing schemes. Fabrication of a ceramic-based nanostructure or metamaterial is challenging to achieve in many existing lithography-based techniques. The bottom-up thin film self-assembly as presented here offers a way to realize all ceramic-based metamaterials, but it is still in its early investigation stage. For example, the materials' chemistry and thermodynamics in terms of oxide−nitride phase stabilities are still under exploration. Overall, it is very promising in terms of designing metamaterials from broad choices of ceramic material candidates with very dissimilar properties.

CONCLUSION

This work presents a nanorod-in-matrix hyperbolic metamaterial coupling all-ceramic components. The vertically aligned NiO nanorods with the average diameter of 6.46 nm possess weak ferromagnetism at room temperature, while the matrix TiN supports a strong surface plasmon mode with field localization at the NiO/TiN interface. Coupling a dissimilar oxide with nitride enables a strong hyperbolic dispersion that covers both 2-fold and 1-fold *k*-space hyperboloids. MO Kerr rotations with light impinging within TiN plasmonic resonance frequencies suggest a strong spin polarization effect at the NiO boundaries, represented by the enhanced coercive field as compared to the magnetic hysteresis loop without optical stimuli. TiN as a refractory ceramic material serves as a robust host matrix to prevent chemical diffusion or interaction. The thin film heterostructure possesses a high epitaxial quality and strained interface upon two-phase coupling. It is flexible in terms of tuning of the secondary phase such as concentration, geometry, and material selection. Such a highly flexible ceramic−ceramic hybrid platform as a hyperbolic metamaterial could offer advantages in terms of low optical losses, chemical inertness, and strong light−matter interactions that hold valuable prospects toward nanophotonic devices, computing, and biosensing.

EXPERIMENTAL SECTION

Sample Fabrication. The NiO−TiN films were grown on single-crystalline MgO (001) substrates using a pulsed laser deposition (PLD) system (Neocera, Lambda Physik Compex Pro 205, KrF excimer laser, λ = 248 nm). The composite target was made by cutting and integrating pure NiO (99.9%) and TiN (99.9%) as a pie-shaped target with a NiO volume ratio of 35%. The pure NiO target was prepared by a conventional sintering and annealing process, and the pure TiN target was purchased from Plasmaterials Inc. The laser beam was focused onto the target at 45° incidence, with an energy density of approximate 3.0 J/cm^2. The growth was carried under high vacuum with a base pressure of 2.0×10^{-6} mbar. Growth temperature was controlled at 650 °C; laser frequency was controlled at 2, 5, and 10 Hz. The cooling rate after the deposition was 15 °C/min.

https://dx.doi.org/10.1021/acs.nanolett.0c02440
Nano Lett. 2020, 20, 6614−6622

Microstructure Characterization. A Panalytical X'Pert X-ray diffractometer with Cu Kα radiation was used for $\theta-2\theta$ characterizations of thin film crystalline quality. SEM EDX is performed on a Quanta 3D FEG microscope with an Oxford Aztec Xstream-2 silicon drift detector with the Xmax80 mm window applied. HAADF STEM imaging and EDX chemical mapping were acquired by the FEI Talos F200X TEM instrument. HRSTEM images were collected using a modified FEI Titan microscope with a hexapole-type illumination aberration corrector. The TEM samples were prepared by the conventional mechanical method, including grinding, dimpling, and ion-milling (PIPS 691 precision ion polishing system, 4.5 keV).

Optical Characterization. Depolarized transmittance (0° incidence) and reflectance spectra (8° incidence) were measured using a Lambda 950 and 1050 UV−vis spectrophotometer. Ellipsometry experiments were carried out on an RC2 spectroscopic ellipsometer (J.A. Woollam Company). Ψ, Δ parameters were collected at 30°, 45°, and 60° incidence in a spectrum range from 350 to 2500 nm. Data fitting was performed using CompleteEase software supported by J.A. Woollam Company. A uniaxial model was built based on four gen-osc oscillators (including three Cody-Lorentz oscillators and one Lorentz oscillator) with Kramers−Kronig (K−K) consistency to ensure the physical accuracy of the fitting.[51] The layer thickness is predefined according to the STEM results. The mean square error (MSE) value is 1.952.

Magnetic and MOKE Characterizations. A magnetic hysteresis loop recording was performed on the magnetic property measurement system (MPMS) from Quantum Design. The measurement was carried out under vibrating sample magnetometer (VSM) mode with the SQUID sensor applied for the measurement. A home-built magneto-optical Kerr effect (MOKE) system was applied, with a He−Ne laser of 632.8 nm at room temperature in a polar and a longitudinal configuration. The incident light is polarized using a linear polarizer; the Kerr rotation of the light is measured using a second polarizer assisted by a photoelastic modulator. In the polar configuration, the reflected light is separated from the normal incident light (0° incident angle) by a 50% beam splitter, and the magnetic field is perpendicular to the film surface. In the longitudinal configuration, the laser has an approximately 30° incidence angle, and the magnetic field is along the intersection of the film plane and the incident plane.

Numerical Simulation. COMSOL Multiphysics software with the Wave Optical module was used for optical simulation. The model was built based on the geometrical parameters taken from STEM micrographs. A 10 nm × 10 nm unit cell was used with periodic boundaries with a mesh size much smaller than the cell dimension. n, k values of NiO and TiN are the fitted ones from ellipsometry measurements. The optical spectra and electric field maps were retrieved based on the model.

■ ASSOCIATED CONTENT

Supporting Information

The Supporting Information is available free of charge at https://pubs.acs.org/doi/10.1021/acs.nanolett.0c02440.

XRD $\theta-2\theta$ scans, histogram of NiO nanorod distribution, SEM EDX mapping and quantification, transmittance with band gap calculation, raw fitting of ellipsometric parameters and polarized reflectance spectra, low-temperature magnetic hysteresis loops, and Kerr rotation of pure NiO film (PDF)

■ AUTHOR INFORMATION

Corresponding Author

Haiyan Wang − *School of Materials Engineering and School of Electrical and Computer Engineering, Purdue University, West Lafayette, Indiana 47907, United States;* orcid.org/0000-0002-7397-1209; Email: hwang00@purdue.edu

Authors

Xuejing Wang − *School of Materials Engineering, Purdue University, West Lafayette, Indiana 47907, United States*

Haohan Wang − *Department of Physics and Astronomy, University of Nebraska—Lincoln, Lincoln, Nebraska 68588, United States*

Jie Jian − *School of Materials Engineering, Purdue University, West Lafayette, Indiana 47907, United States*

Bethany X. Rutherford − *School of Materials Engineering, Purdue University, West Lafayette, Indiana 47907, United States;* orcid.org/0000-0003-4149-9891

Xingyao Gao − *School of Materials Engineering, Purdue University, West Lafayette, Indiana 47907, United States*

Xiaoshan Xu − *Department of Physics and Astronomy, University of Nebraska—Lincoln, Lincoln, Nebraska 68588, United States;* orcid.org/0000-0002-4363-392X

Xinghang Zhang − *School of Materials Engineering, Purdue University, West Lafayette, Indiana 47907, United States;* orcid.org/0000-0002-8380-8667

Complete contact information is available at: https://pubs.acs.org/10.1021/acs.nanolett.0c02440

Notes

The authors declare no competing financial interest.

■ ACKNOWLEDGMENTS

This work was supported by the U.S. National Science Foundation (DMR-2016453 for thin film processing and DMR-1565822 for the high-resolution TEM and STEM effort). This work was partially supported by the Basil R. Turner Professorship at Purdue University. Work at the Molecular Foundry was supported by the Office of Science, Office of Basic Energy Sciences, of the U.S. Department of Energy under Contract DE-AC02-05CH11231. H.H.W. and X.X. acknowledge the support from U.S. National Science Foundation, DMR-1454618.

■ REFERENCES

(1) Zheludev, N. I.; Kivshar, Y. S. From metamaterials to metadevices. *Nat. Mater.* **2012**, *11* (11), 917−924.

(2) He, Q.; Sun, S.; Zhou, L. Tunable/Reconfigurable Metasurfaces: Physics and Applications. *Research* **2019**, *2019*, 16.

(3) Schuller, J. A.; Barnard, E. S.; Cai, W. S.; Jun, Y. C.; White, J. S.; Brongersma, M. L. Plasmonics for extreme light concentration and manipulation. *Nat. Mater.* **2010**, *9* (3), 193−204.

(4) Smith, D. R.; Pendry, J. B.; Wiltshire, M. C. K. Metamaterials and Negative Refractive Index. *Science* **2004**, *305* (5685), 788−792.

(5) Kabashin, A. V.; Evans, P.; Pastkovsky, S.; Hendren, W.; Wurtz, G. A.; Atkinson, R.; Pollard, R.; Podolskiy, V. A.; Zayats, A. V. Plasmonic nanorod metamaterials for biosensing. *Nat. Mater.* **2009**, *8* (11), 867−871.

(6) Rho, J.; Ye, Z.; Xiong, Y.; Yin, X.; Liu, Z.; Choi, H.; Bartal, G.; Zhang, X. Spherical hyperlens for two-dimensional sub-diffractional imaging at visible frequencies. *Nat. Commun.* **2010**, *1* (1), 143.

(7) Cortes, C. L.; Newman, W.; Molesky, S.; Jacob, Z. Quantum nanophotonics using hyperbolic metamaterials. *J. Opt.* **2012**, *14* (6), 15.
(8) Ferrari, L.; Wu, C. H.; Lepage, D.; Zhang, X.; Liu, Z. W. Hyperbolic metamaterials and their applications. *Prog. Quantum Electron.* **2015**, *40*, 1−40.
(9) Lapine, M.; Shadrivov, I. V.; Kivshar, Y. S. Colloquium: Nonlinear metamaterials. *Rev. Mod. Phys.* **2014**, *86* (3), 1093−1123.
(10) Shalaev, V. M. Optical negative-index metamaterials. *Nat. Photonics* **2007**, *1* (1), 41−48.
(11) Khurgin, J. B. How to deal with the loss in plasmonics and metamaterials. *Nat. Nanotechnol.* **2015**, *10* (1), 2−6.
(12) Khurgin, J. B.; Boltasseva, A. Reflecting upon the losses in plasmonics and metamaterials. *MRS Bull.* **2012**, *37* (8), 768−779.
(13) West, P. R.; Ishii, S.; Naik, G. V.; Emani, N. K.; Shalaev, V. M.; Boltasseva, A. Searching for better plasmonic materials. *Laser & Photonics Reviews* **2010**, *4* (6), 795−808.
(14) Naik, G. V.; Shalaev, V. M.; Boltasseva, A. Alternative Plasmonic Materials: Beyond Gold and Silver. *Adv. Mater.* **2013**, *25* (24), 3264−3294.
(15) Boltasseva, A.; Atwater, H. A. Low-Loss Plasmonic Metamaterials. *Science* **2011**, *331* (6015), 290−291.
(16) Iorsh, I. V.; Mukhin, I. S.; Shadrivov, I. V.; Belov, P. A.; Kivshar, Y. S. Hyperbolic metamaterials based on multilayer graphene structures. *Phys. Rev. B: Condens. Matter Mater. Phys.* **2013**, *87* (7), 075416.
(17) Kravets, V. G.; Jalil, R.; Kim, Y. J.; Ansell, D.; Aznakayeva, D. E.; Thackray, B.; Britnell, L.; Belle, B. D.; Withers, F.; Radko, I. P.; Han, Z.; Bozhevolnyi, S. I.; Novoselov, K. S.; Geim, A. K.; Grigorenko, A. N. Graphene-protected copper and silver plasmonics. *Sci. Rep.* **2015**, *4* (1), 5517.
(18) Catellani, A.; Calzolari, A. Plasmonic properties of refractory titanium nitride. *Phys. Rev. B: Condens. Matter Mater. Phys.* **2017**, *95* (11), 10.
(19) Li, W.; Guler, U.; Kinsey, N.; Naik, G. V.; Boltasseva, A.; Guan, J. G.; Shalaev, V. M.; Kildishev, A. V. Refractory Plasmonics with Titanium Nitride: Broadband Metamaterial Absorber. *Adv. Mater.* **2014**, *26* (47), 7959.
(20) Jahani, S.; Jacob, Z. All-dielectric metamaterials. *Nat. Nanotechnol.* **2016**, *11* (1), 23−36.
(21) Wu, Y. Z.; Qiu, Z. Q.; Zhao, Y.; Young, A. T.; Arenholz, E.; Sinkovic, B. Tailoring the spin direction of antiferromagneticNiOthin films grown on vicinalAg(001). *Phys. Rev. B: Condens. Matter Mater. Phys.* **2006**, *74* (21), 212402.
(22) Finazzi, M.; Brambilla, A.; Biagioni, P.; Graf, J.; Gweon, G. H.; Scholl, A.; Lanzara, A.; Duò, L. Interface Coupling Transition in a Thin Epitaxial Antiferromagnetic Film Interacting with a Ferromagnetic Substrate. *Phys. Rev. Lett.* **2006**, *97* (9), 097202.
(23) Adhikary, J.; Chakraborty, P.; Das, B.; Datta, A.; Dash, S. K.; Roy, S.; Chen, J.-W.; Chattopadhyay, T. Preparation and characterization of ferromagnetic nickel oxide nanoparticles from three different precursors: application in drug delivery. *RSC Adv.* **2015**, *5* (45), 35917−35928.
(24) Ravikumar, P.; Kisan, B.; Perumal, A. *AIP Adv.* **2015**, *5* (8), 087116.
(25) Bi, H.; Li, S.; Zhang, Y.; Du, Y. Ferromagnetic-like behavior of ultrafine NiO nanocrystallites. *J. Magn. Magn. Mater.* **2004**, *277* (3), 363−367.
(26) González-Díaz, J. B.; García-Martín, A.; Armelles, G.; Navas, D.; Vázquez, M.; Nielsch, K.; Wehrspohn, R. B.; Gösele, U. Enhanced Magneto-Optics and Size Effects in Ferromagnetic Nanowire Arrays. *Adv. Mater.* **2007**, *19* (18), 2643−2647.
(27) Maksymov, I. S. Magneto-plasmonic nanoantennas: Basics and applications. *Reviews in Physics* **2016**, *1*, 36−51.
(28) Manera, M. G.; Colombelli, A.; Taurino, A.; Martin, A. G.; Rella, R. Magneto-Optical properties of noble-metal nanostructures: functional nanomaterials for bio sensing. *Sci. Rep.* **2018**, *8* (1), 12640.
(29) Armelles, G.; Cebollada, A.; Garcia-Martin, A.; Gonzalez, M. U. Magnetoplasmonics: Combining Magnetic and Plasmonic Functionalities. *Adv. Opt. Mater.* **2013**, *1* (1), 10−35.
(30) Armelles, G.; Cebollada, A.; Garcia-Martin, A.; Garcia-Martin, J. M.; Gonzalez, M. U.; Gonzalez-Diaz, J. B.; Ferreiro-Vila, E.; Torrado, J. F. Magnetoplasmonic nanostructures: systems supporting both plasmonic and magnetic properties. *J. Opt. A: Pure Appl. Opt.* **2009**, *11* (11), 10.
(31) Wang, H.; Tiwari, A.; Kvit, A.; Zhang, X.; Narayan, J. Epitaxial growth of TaN thin films on Si(100) and Si(111) using a TiN buffer layer. *Appl. Phys. Lett.* **2002**, *80* (13), 2323−2325.
(32) Narayan, J.; Tiwari, P.; Chen, X.; Singh, J.; Chowdhury, R.; Zheleva, T. Epitaxial-growth of TiN films on (100) silicon substrates by laser physical vapor-deposition. *Appl. Phys. Lett.* **1992**, *61* (11), 1290−1292.
(33) Perez-Casero, R.; Perriere, J.; Gutierrez-Llorente, A.; Defourneau, D.; Millon, E.; Seiler, W.; Soriano, L. Thin films of oxygen-deficient perovskite phases by pulsed-laser ablation of strontium titanate. *Phys. Rev. B: Condens. Matter Mater. Phys.* **2007**, *75* (16), 7.
(34) Millon, E.; Nistor, M.; Hebert, C.; Davila, Y.; Perriere, J. Phase separation in nanocomposite indium tin oxide thin films grown at room temperature: on the role of oxygen deficiency. *J. Mater. Chem.* **2012**, *22* (24), 12179−12185.
(35) Su, Q.; Yoon, D.; Sisman, Z.; Khatkhatay, F.; Jia, Q.; Manthiram, A.; Wang, H. Vertically aligned nanocomposite La0.8Sr0.2MnO3-δ/Zr0.92Y0.08O1.96 thin films as electrode/electrolyte interfacial layer for solid oxide reversible fuel cells. *Int. J. Hydrogen Energy* **2013**, *38* (36), 16320−16327.
(36) Zhang, D.; Misra, S.; Li, L.; Wang, X.; Jian, J.; Lu, P.; Gao, X.; Sun, X.; Qi, Z.; Kalaswad, M.; Zhang, X.; Wang, H. Tunable Optical Properties in Self-Assembled Oxide-Metal Hybrid Thin Films via Au-Phase Geometry Control: From Nanopillars to Nanodisks. *Adv. Opt. Mater.* **2020**, *8* (4), 1901359.
(37) Chen, A. P.; Su, Q.; Han, H.; Enriquez, E.; Jia, Q. X. Metal Oxide Nanocomposites: A Perspective from Strain, Defect, and Interface. *Adv. Mater.* **2019**, *31* (4), 30.
(38) Wang, X.; Jian, J.; Diaz-Amaya, S.; Kumah, C. E.; Lu, P.; Huang, J.; Lim, D. G.; Pol, V. G.; Youngblood, J. P.; Boltasseva, A.; Stanciu, L. A.; O'Carroll, D. M.; Zhang, X.; Wang, H. Hybrid plasmonic Au−TiN vertically aligned nanocomposites: a nanoscale platform towards tunable optical sensing. *Nanoscale Advances* **2019**, *1* (3), 1045−1054.
(39) Wang, X.; Jian, J.; Zhou, Z.; Fan, C.; Dai, Y.; Li, L.; Huang, J.; Sun, J.; Donohue, A.; Bermel, P.; Zhang, X.; Chen, H. T.; Wang, H. Self-Assembled Ag−TiN Hybrid Plasmonic Metamaterial: Tailorable Tilted Nanopillar and Optical Properties. *Adv. Opt. Mater.* **2019**, *7* (3), 1801180.
(40) Naik, G. V.; Schroeder, J. L.; Ni, X.; Kildishev, A. V.; Sands, T. D.; Boltasseva, A. Titanium nitride as a plasmonic material for visible and near-infrared wavelengths. *Opt. Mater. Express* **2012**, *2* (4), 478.
(41) Wang, X.; Ma, X.; Shi, E.; Lu, P.; Dou, L.; Zhang, X.; Wang, H. Large-Scale Plasmonic Hybrid Framework with Built-In Nanohole Array as Multifunctional Optical Sensing Platforms. *Small* **2020**, *16* (11), 1906459.
(42) Shekhar, P.; Atkinson, J.; Jacob, Z. Hyperbolic metamaterials: fundamentals and applications. *Nano Convergence* **2014**, *1* (1), 14.
(43) Maas, R.; Parsons, J.; Engheta, N.; Polman, A. Experimental realization of an epsilon-near-zero metamaterial at visible wavelengths. *Nat. Photonics* **2013**, *7* (11), 907−912.
(44) Zhang, W.; Li, J.; Ding, X.; Pernod, P.; Tiercelin, N.; Song, Y. Tunable Magneto-Optical Kerr Effects of Nanoporous Thin Films. *Sci. Rep.* **2017**, *7* (1), 2888.
(45) Lodewijks, K.; Maccaferri, N.; Pakizeh, T.; Dumas, R. K.; Zubritskaya, I.; Åkerman, J.; Vavassori, P.; Dmitriev, A. Magneto-plasmonic Design Rules for Active Magneto-Optics. *Nano Lett.* **2014**, *14* (12), 7207−7214.
(46) Rollinger, M.; Thielen, P.; Melander, E.; Östman, E.; Kapaklis, V.; Obry, B.; Cinchetti, M.; García-Martín, A.; Aeschlimann, M.;

https://dx.doi.org/10.1021/acs.nanolett.0c02440
Nano Lett. 2020, 20, 6614−6622

Papaioannou, E. T. Light Localization and Magneto-Optic Enhancement in Ni Antidot Arrays. *Nano Lett.* **2016**, *16* (4), 2432−2438.
(47) Jayakumar, O. D.; Mandal, B. P.; Majeed, J.; Lawes, G.; Naik, R.; Tyagi, A. K. Inorganic−organic multiferroic hybrid films of Fe3O4 and PVDF with significant magneto-dielectric coupling. *J. Mater. Chem. C* **2013**, *1* (23), 3710.
(48) Chu, Y.-H.; Martin, L. W.; Holcomb, M. B.; Gajek, M.; Han, S.-J.; He, Q.; Balke, N.; Yang, C.-H.; Lee, D.; Hu, W.; Zhan, Q.; Yang, P.-L.; Fraile-Rodríguez, A.; Scholl, A.; Wang, S. X.; Ramesh, R. Electric-field control of local ferromagnetism using a magnetoelectric multiferroic. *Nat. Mater.* **2008**, *7* (6), 478−482.
(49) Dulub, O.; Batzilln, M.; Solovev, S.; Loginova, E.; Alchagirov, A.; Madey, T. E.; Diebold, U. *Science (Washington, DC, U. S.)* **2007**, *317* (5841), 1052−1056.
(50) Wang, D.; Su, D. S.; Schlögl, R. *Z. Anorg. Allg. Chem.* **2004**, *630* (7), 1007−1014.
(51) Shahrokhabadi, H.; Bananej, A.; Vaezzadeh, M. Investigation of Cody−Lorentz and Tauc−Lorentz Models in Characterizing Dielectric Function of (HfO2) x (ZrO2)1−x Mixed Thin Film. *J. Appl. Spectrosc.* **2017**, *84* (5), 915−922.

https://dx.doi.org/10.1021/acs.nanolett.0c02440
Nano Lett. 2020, 20, 6614−6622